



Anchored Co-oxo generated by cobalt single atoms outperformed aqueous species from the counterparts in peroxymonosulfate treatment

Zi-Jie Xiao^a, Bai-Qin Zhou^a, Xiao-Chi Feng^{a,*}, Hong-Tao Shi^a, Yi-Ning Zhu^a, Cai-Peng Wang^a, Bart Van der Bruggen^b, Nan-Qi Ren^a

^a State Key Laboratory of Urban Water Resource and Environment, School of Civil and Environmental Engineering, Harbin Institute of Technology (Shenzhen), Shenzhen, Guangdong 518055, PR China

^b Department of Chemical Engineering, KU Leuven, 3001 Leuven, Belgium

ARTICLE INFO

Keywords:

Single atoms
High-valent metal-oxo
Transition state
Active species

ABSTRACT

How single-atom (SA) materials trigger highly efficient catalysis in peroxymonosulfate (PMS) treatment is not fully understood. In this study, cobalt SA sites were fabricated as a PMS activator for antibiotic degradation and compared with cobalt nanoparticles (NPs). Co-SA/PMS showed superior degradation efficiency, adaptability, and stability to Co-NP/PMS in antibiotic treatment. Identification of the reactive species suggested that Co-SA/PMS were privileged from generating anchored high-valent Co-oxo (Co=O) species for triggering interface oxidation, while Co-NP/PMS generated aqueous radical and non-radical species with less reliability. Theoretical calculations and extended experiments of the oxidation effects showed that Co=O is more stable for Co-SAs than for Co-NPs, providing better accessibility to accomplish interface oxygen transfer. Furthermore, oxidation of different antibiotic contaminants and various typical sulfadoxin degradation pathways were investigated to distinguish the effects of the different pathways. Overall, this study shows the activation improvement caused by different existential forms of cobalt in PMS treatment.

1. Introduction

Peroxydisulfate (PMS) has been demonstrated to be a promising oxidizer to overcome various technical limitations of H₂O₂ for removal of environmental pollutants (PPCPs) [1,2]. Because pharmaceuticals and personal care products pose threats to human health and the environment, PMS treatment of PPCPs has been well studied because of its effective degradation performance [3,4]. Transition metals have been widely applied to PMS system activation, among which Co²⁺ shows the greatest potential [5]. However, homogeneous catalysts are considered to be secondary pollutants of the environment, and thus separable heterogeneous catalysts have been developed by anchoring transition metals to non-soluble matrices [6]. Heterogeneous PMS-treatment methods generate various active species through catalytic activation [7]. Radical pathways are useful in contaminant degradation, in which various free radicals, such as sulfate radicals (SO₄^{•-}) and hydroxyl radicals (•OH), play crucial roles [8,9]. Singlet oxygen (¹O₂), an effective non-radical species for oxidation, has also proved to be effective in heterogeneous PMS treatment [10]. Furthermore, as an interface

oxidation species, high-valent metal-oxo (Co=O) is an anchored active species for stable oxidation [11]. Co=O has been focused on because of its high efficiency and adaptability, but it is still far from clear how metal-based catalysts generate this interface oxidation pathway.

Different active species show selective oxidative degradation capabilities for different types of pollutants. Therefore, numerous catalysts have been investigated for PMS activation to generate different active species for selective oxidation of contaminants [12]. Desired oxidation pathways can be accessed by modifying the catalysts in PMS activation systems [13,14]. To achieve high degradation ability in PMS treatment, it is important to select appropriate oxidation pathways originating from a specific catalyst, and thus methods for developing and modifying the optimal catalyst material are essential. Single-atom (SA) composite catalysts are a type of heterogeneous catalyst formed by atomically dispersing active metal centers on a matrix [15]. Co-SA composite catalysts show excellent performance in PMS activation for removal of environmental contaminants because of their highly reactive and stable catalysis performance [16]. Various PMS-activation mechanisms induced by SA catalysts have been proposed to explain efficient

* Correspondence to: Harbin Institute of Technology, Shenzhen, PR China.

E-mail address: fengxiaochi@hit.edu.cn (X.-C. Feng).

<https://doi.org/10.1016/j.apcatb.2023.122483>

Received 20 January 2023; Received in revised form 11 February 2023; Accepted 16 February 2023

Available online 19 February 2023

0926-3373/© 2023 Elsevier B.V. All rights reserved.

degradation of contaminants, including radical pathways, [17] $^1\text{O}_2$, [18] and $\text{Co}=\text{O}$ [19]. The reported oxidation pathways have been continuously updated owing to the rapid development of SA-anchored matrices and clarification of once-overlooked mechanisms.

Research has focused on modification of SA catalysts to realize different activation mechanisms for selective degradation [20,21]. In the SA synthesis process, nanoparticles (NPs) are a common byproduct of catalyst structuring [22]. Specifically, for the same metal-based active centers and anchoring matrices, the active sites impose a size effect on PMS activation, which could further contribute to a change in the active species [23]. Because different activation mechanisms can cause different degradation performance, it is important to clarify the transformation mechanism of the active species induced by different active sites. Investigation of selective PMS systems with SAs and NPs not only reveals how the active sites change the activation mechanism, but it also helps to develop the required degradation systems for different pollutants. Previous studies have shown the difference of the PMS activation mechanisms of SAs and NPs by investigating the changes in the Gibbs energy of PMS cleavage [24]. Although various studies have investigated the difference between SAs and NPs for PMS activation, further investigation of methods for catalyst modification to change generation of the active species and cause pathway transformation is still required.

In this study, Co-SA sites were constructed on biochar matrices through calcination with an extra nitrogen source, and accordingly cobalt NPs were prepared on the same matrices for comparison. The Co-SA/biochar composite (hereafter, Co-SA) showed better performance and adaptability than the Co-NP/biochar composite (hereafter, Co-NP) for PMS activation in contaminant degradation, because the Co-SA activated PMS to generate anchored $\text{Co}=\text{O}$ species while the Co-NP produced aqueous reactive species as the dominant oxidation pathways. Furthermore, the mechanisms for generating different active species were explained by theoretical calculations, and the difference in the oxidation effect was illustrated by degradation of various contaminants and for various degradation pathways of a specific contaminant. This study was conducted as follows: (I) The accessibility for constructing Co-SA sites on the biochar matrix through two-step calcination was demonstrated. (II) Preparation conditions were determined to compare Co-SA and Co-NP for activating PMS to degrade sulfadoxin along with characterization and performance analysis. (III) The active species in the Co-SA/PMS and Co-NP/PMS systems were identified, showing the relationship between the Co morphology and catalysis mechanism. (IV) The presence of different activation mechanisms was explained by transition-state calculation of $\text{Co}=\text{O}$ generation, and the differences of the oxidation effects of various contaminants and for various degradation pathways of sulfadoxin were evaluated to show the oxidation effects of different oxidation mechanisms.

2. Materials and methods

2.1. Reagents

Potassium peroxydisulfate ($\text{KHSO}_5 \cdot 0.5\text{KHSO}_4 \cdot 0.5\text{K}_2\text{SO}_4$, PMS, $\geq 47\%$), potassium thiocyanate (KSCN, 99 %), 2,2,6,6-tetramethylpiperidine (TEMP, 99 %), and 5,5-dimethyl-1-pyrroline *N*-oxide (DMPO, 98 %) were obtained from Aladdin Biochemical Technology Co., Ltd (Shanghai, China). Sodium thiosulfate ($\text{Na}_2\text{S}_2\text{O}_3 \cdot 5\text{H}_2\text{O}$, $\geq 99\%$), sulfuric acid (H_2SO_4 , 98 %), and sodium hydroxide (NaOH, $\geq 98\%$) were purchased from Hushi Laboratorial Equipment Co., Ltd (Shanghai, China). Ethanol (EtOH , $\geq 99\%$), methanol (MeOH , $\geq 99\%$), furfuryl alcohol (FFA, $\geq 99\%$), phenyl methyl sulfoxide (PMSO, 98 %), phenyl methyl sulfone (PMSO_2 , 98 %) cobalt nitrate ($\text{Co}(\text{NO}_3)_2 \cdot 6\text{H}_2\text{O}$, AR), sodium bicarbonate (NaHCO_3 , $\geq 99.8\%$), sodium hydroxide (NaOH, $\geq 99\%$), sodium phosphate dibasic (Na_2HPO_4 , 99 %), and sodium chloride (NaCl, 99.5 %) were acquired from Macklin Biochemical Co., Ltd (Shanghai, China). The sources of the target contaminants are given in Table S1.

2.2. Synthesis

Biochar, as the material substrate, was prepared by calcination of walnut shells (purchased from a farm in Shenzhen, China). The walnut shells (10 g) were finely crushed into a powder and stuffed in a combustion boat with a cover for calcination in a muffle furnace. The heating rate was set to $10^\circ\text{C}/\text{min}$, and after the calcination temperature reached 700°C , the furnace was maintained at this temperature for 8 h. Co-SA was prepared by the carbonization method, with adsorption of cobalt ions and external nitrogen doping. Biochar (1 g) was immersed in 100 mL of $\text{Co}(\text{NO}_3)_2$ solution (concentration of 1 g/L) and stirred for 24 h to reach the adsorption-desorption equilibrium. Subsequently, the biochar was filtered and dried, mixed with 10 g of an additional nitrogen source (DCD), and carbonized in a tube furnace under a high-purity argon atmosphere. The as-prepared sample was then heated to 550°C at $5^\circ\text{C}/\text{min}$ under pure N_2 flow, kept at 550°C for 6 h, and then heated to 1000°C at $10^\circ\text{C}/\text{min}$ in the same atmosphere. The as-obtained samples were collected and pickled with 1 M H_2SO_4 for 12 h to remove possible cobalt nanoparticles, and they were then washed repeatedly with deionized water until the pH of the eluent was neutral. Finally, the samples were placed in a vacuum drying oven at 60°C overnight and then removed for use.

2.3. Characterization

The crystalline structures of the as-synthesized samples were investigated by X-ray diffraction (XRD) using a Rigaku Ultima IV X-ray diffractometer with $\text{Cu K}\alpha$ radiation ($\lambda = 1.5406 \text{ \AA}$) in the 2θ range from 5° to 90° . X-ray photoelectron spectroscopy (XPS) was performed to measure the valence states of the constituent elements (Thermo Scientific K-Alpha). The X-ray absorption fine structure (XAFS) spectra (Co K-edge) were collected at beamline BL44B2 of the SPring-8 synchrotron in Japan. The storage rings of SPring-8 were operated at 8.0 GeV with a maximum current of 250 mA using a Si(111) double-crystal monochromator, and data collection was performed in transmission mode using an ionization chamber. Vibrating sample magnetometry (VSM, Lakeshore 7404) was performed to identify the magnetic hysteresis loops of the materials. The morphological and textural properties were determined by scanning electron microscopy (SEM, Hitachi SU8010 FE-SEM) using an Al $\text{K}\alpha$ X-ray source and transmission electron microscopy (TEM, FEI Talos F200X) with a SuperXG2 source. An aberration-corrected high-angle annular dark-field scanning transmission electron microscope (HAADF-STEM, JEOL ARM 300F) equipped with double aberration correctors and a cold field emission gun operated at 80 kV was used for detection of dispersion of cobalt. The surface properties and functional groups were identified by Fourier transform infrared (FTIR) spectrometry (Thermo Scientific Nicolet iN10). Raman spectroscopy (WITec alpha 300R) was performed to investigate the structures and properties of graphene, and the specific surface areas and pore-size distributions of the materials were determined by the Brunauer-Emmett-Teller (BET) method (Micromeritics ASAP 2460) in a N_2 atmosphere. To detect the various active species in the PMS systems, electron paramagnetic resonance (EPR) spectroscopy (Bruker EMXplus) was performed with trapping agents.

2.4. Experiments and analysis

The degradation experiments were initiated by simultaneous addition of PMS (0.5 mM) and catalyst (100 mg/L) to the contaminant solution (100 mL, 0.05 M). At specific intervals, samples were taken and immediately quenched by addition of 25 μL of saturated sodium thiosulfate solution and then filtered through a $0.22\text{-}\mu\text{m}$ Teflon-membrane filter. All of the experiments were conducted in triplicate. The concentrations of all of the contaminants were determined by an ultra-performance liquid chromatograph (ACQUITY H-Class, Waters, Milford, MA) equipped with a C18 column ($2.1 \text{ mm} \times 100 \text{ mm}$, $1.8 \mu\text{m}$) and

an ultraviolet detector. The column temperature was $40\text{ }^{\circ}\text{C} \pm 1.0\text{ }^{\circ}\text{C}$. The representative contaminant sulfadoxin was detected in the mobile phase with a mixture of 40 % acetonitrile and 60 % H_2O at a flow rate of 0.3 mL min^{-1} with a detection wavelength of 275 nm. The methods for detecting the other contaminants are given in Table S1. Identification of PMSO and its oxidation product PMSO₂ was performed by gas chromatography with mass spectrometry (GC-MS, Agilent 5977 C). The intermediates were identified by the UPLC-MS/MS (AB SCIEX, Triple Quad 4500) under the same conditions as for the UPLC, which were first pretreated by solid extraction.

2.5. Theoretical methods

GaussView was used to obtain the molecular structures of the contaminants, and structural optimization and calculation of the molecular descriptors were performed with Gaussian 16. The molecular structures were optimized using the M06–2X hybrid functional with the def2-SVP basis set, including the atom-pairwise dispersion (DFT-D3) correction, and the descriptors were calculated at the M06–2X/def2-TZVP level [25, 26]. An ultrafine grid was used for the electron density together with tight SCF convergence criteria. Because all of the contaminant degradation experiments were performed in aqueous solution, IEFPCM was

considered as the implicit water solvation model for geometric optimization, and SMD was used for the single-point energy calculations [27]. The descriptors used are defined in Table S2.

The Gibbs energy change of PMS adsorption and cleavage was calculated with the Vienna ab initio Simulation Program (VASP) [28, 29]. The generalized gradient approximation (GGA) in the Perdew–Burke–Ernzerhof (PBE) form with a cutoff energy of 500 eV for the planewave basis set was used [30]. A $5 \times 5 \times 1$ Monkhorst–Pack grid was used for sampling the Brillouin zone in structure optimization [31]. The ion–electron interactions were described by the projector augmented-wave (PAW) method [32]. The convergence criteria for structure optimization were a maximum force on each atom of less than 0.01 eV/\AA with an energy change of less than $1 \times 10^{-5}\text{ eV}$. The DFT-D3 semiempirical correction was described by Grimme’s scheme method [33]. The Gibbs free energy change (ΔG) for each elemental step is defined in Text S1.

3. Results and discussion

3.1. Structuring the cobalt single atom sites

Two-stage calcination was performed to construct the Co-SA sites

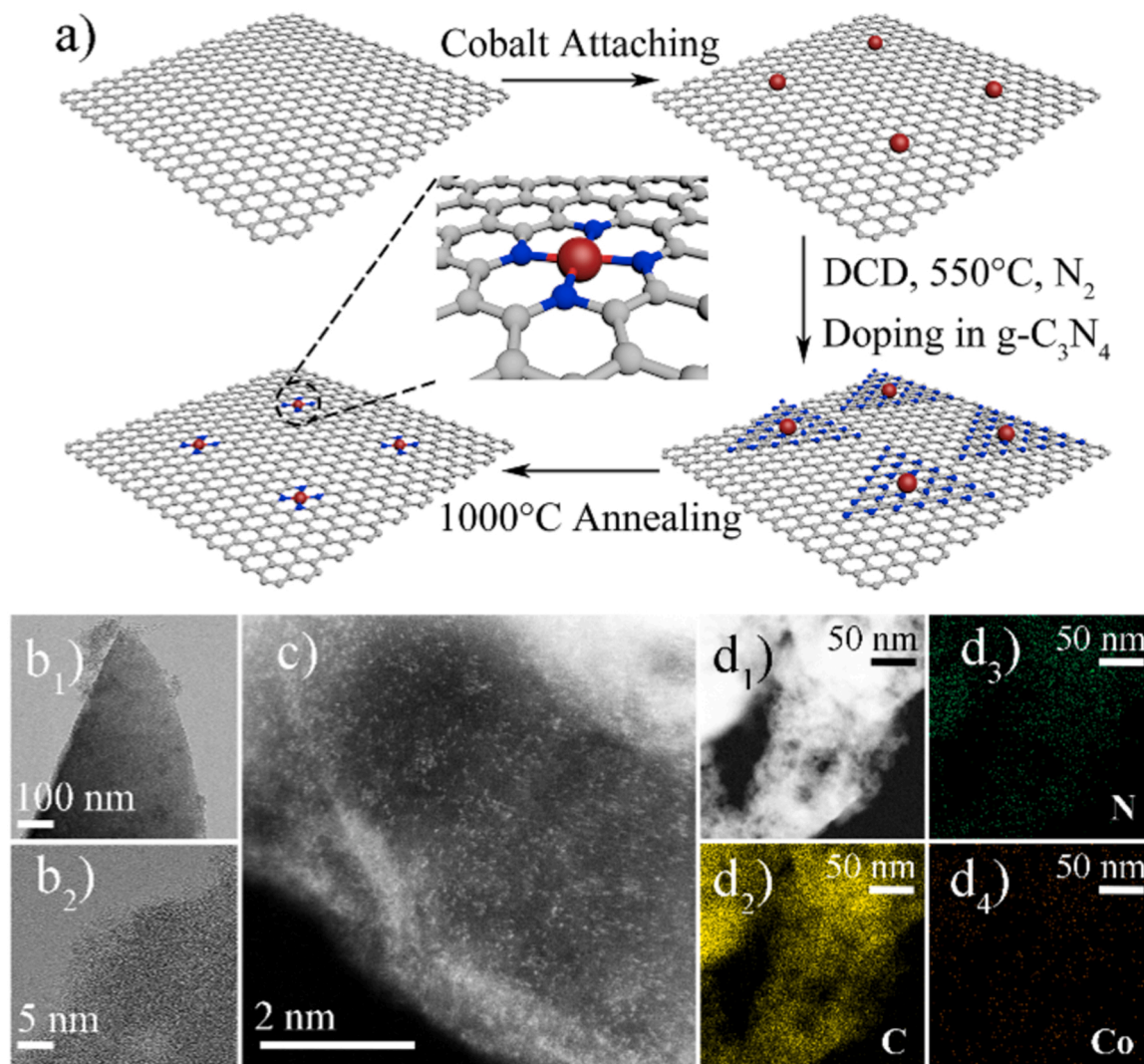


Fig. 1. a) Schematic illustration of structuring cobalt single-atom sites on the biochar matrix through the two-stage carbonization procedure. b) High-resolution transmission electron microscopy images. c) High-angle annular dark-field scanning transmission electron microscopy image. d) Energy dispersive spectroscopy elemental mapping of C, N, and Co. All of the samples were prepared under the optimal synthesis conditions.

(Fig. 1a). In the first stage, the adsorbed Co atoms were transformed to Co-C₃N₄ by melting and rearrangement of dicyandiamide (DCD) at 550 °C for 6 h under N₂ protection [34]. In the second stage, C₃N₄ was decomposed and volatilized in a furnace at 1000 °C for 2 h, while the Co-N_x SA sites remained anchored to the biochar matrix [35]. SEM images of the Co-biochar materials under the optimal and control synthesis conditions are shown in Fig. S1, which indicated that changing the synthesis conditions did not necessarily change the material surface. High-resolution TEM images showed that the material had a smooth surface and an amorphous structure (Fig. 1b). HAADF-STEM showed that individual Co atoms were clearly anchored to the biochar matrix (Fig. 1c). C₃N₄, the critical medium for formation of Co-SA sites, was derived from carbonization of DCD at 550 °C for 6 h, which kept the spatial intervals of the Co atoms. When the furnace was heated to 1000 °C, C₃N₄ deformed while the Co atoms remained in the form of Co-N_x, which was homogeneously anchored to and stabilized on the biochar matrix (Fig. 1d) [36,37].

To analyze the atomic structure of Co on the matrix, X-ray absorption fine structure (XAFS) spectroscopy was performed to analyze the as-synthesized Co-SA with cobalt phthalocyanine (CoPc), CoO, and Co foil as references. The X-ray absorption near-edge structure (XANES) spectra revealed that the rising edge of Co-SA was situated between the edge of Co foil and CoPc (Fig. 2a), indicating that the average valence state of the Co-SA sites was between 0 and +2 [38]. The XANES first derivatives and Fourier-transformed (FT) extended XAFS (EXAFS) fitting curves in *k* space is shown in Fig. 2c and d, and analysis of the EXAFS fitting is summarized in Table S3. The FT *k*³-weighted EXAFS spectra showed that the peaks of the Co-SA sites and CoPc shared the same position at 1.5 Å (Fig. 2b), which is attributed to the Co-N coordination

of the Co-SA sites. No peaks of Co-O at 1.7 Å and Co-Co bonding at 2.1 Å were detected for Co-SA, showing no generation of Co NPs [39]. The wavelet transform (WT) contour plot of Co-SA is shown in Fig. 2e, revealing a WT maximum at 4.2 Å⁻¹ corresponding to Co-N bonding, while intensities of the maximum at 7.1 Å⁻¹ and the maximum at 3.5 Å⁻¹ corresponding to Co-Co and Co-O bonding were not observed [40]. The EXAFS fitting results revealed that the first shell of the Co atom had a coordination number of approximately 4, suggesting that the Co atom was on average coordinated to four N atoms to form the Co-N₄ structure (Fig. 2f) [41]. Therefore, the two-stage calcination process with an external N source successfully constructed Co-SA sites on the biochar matrix, providing a potential PMS activator for contaminant degradation.

3.2. Regulation and performance of single atoms and nanoparticles

To investigate the effect of the preparation conditions on the atomic structure of Co in the materials and the corresponding performance, the preparation conditions of the initial concentration for Co adsorption (0–5 g/L), residence time at 550 °C (0–6 h), and type of external N source (DCD, melamine, and urea) were varied to synthesize control groups for comparison (Fig. 3a–c). Co-SA sites were synthesized under the optimal preparation conditions: initial Co-ion concentration for adsorption of 1 g/L, residence time for 550 °C heating of 6 h, and type of external N source of DCD. When the initial Co concentration was 0 g/L (i.e., no Co was attached to the biochar before carbonization), the prepared material showed almost no catalytic performance compared with the system with only PMS addition. The performance increased as the initial concentration of Co increased until 1 g/L, and even when it

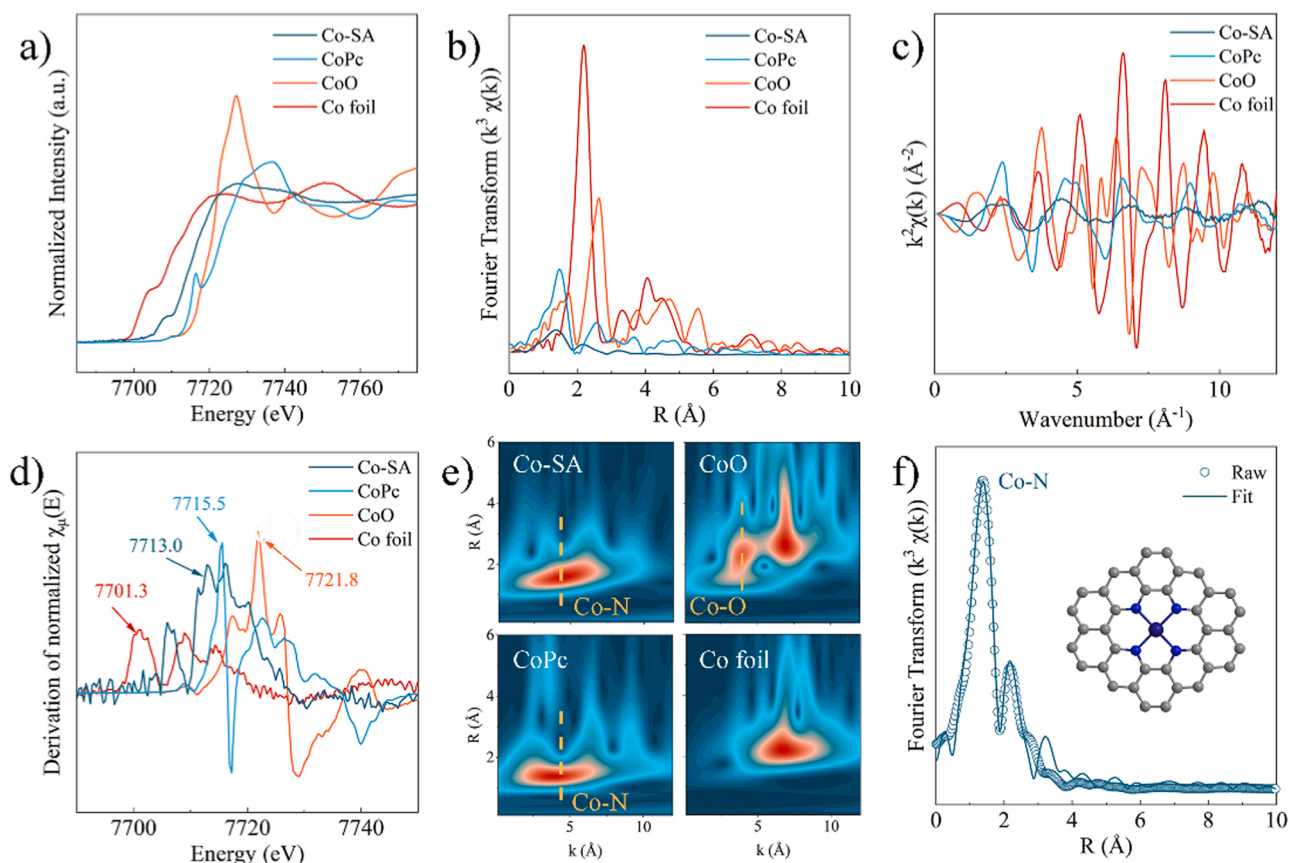


Fig. 2. a) Normalized Co K-edge X-ray absorption near-edge structure (XANES) spectra, b) *k*³-weighted Fourier-transformed (FT) spectra from the Co K-edge extended X-ray absorption fine structure (EXAFS) spectra, c) XANES first derivatives, d) FT-EXAFS fitting curves in *k* space, and e) wavelet transform of the EXAFS of the Co-based sample and references (CoPc, CoO, and Co foil). f) Corresponding EXAFS R-space fitting curves of the Co-based sample and the proposed Co-N₄ structure on the sample.

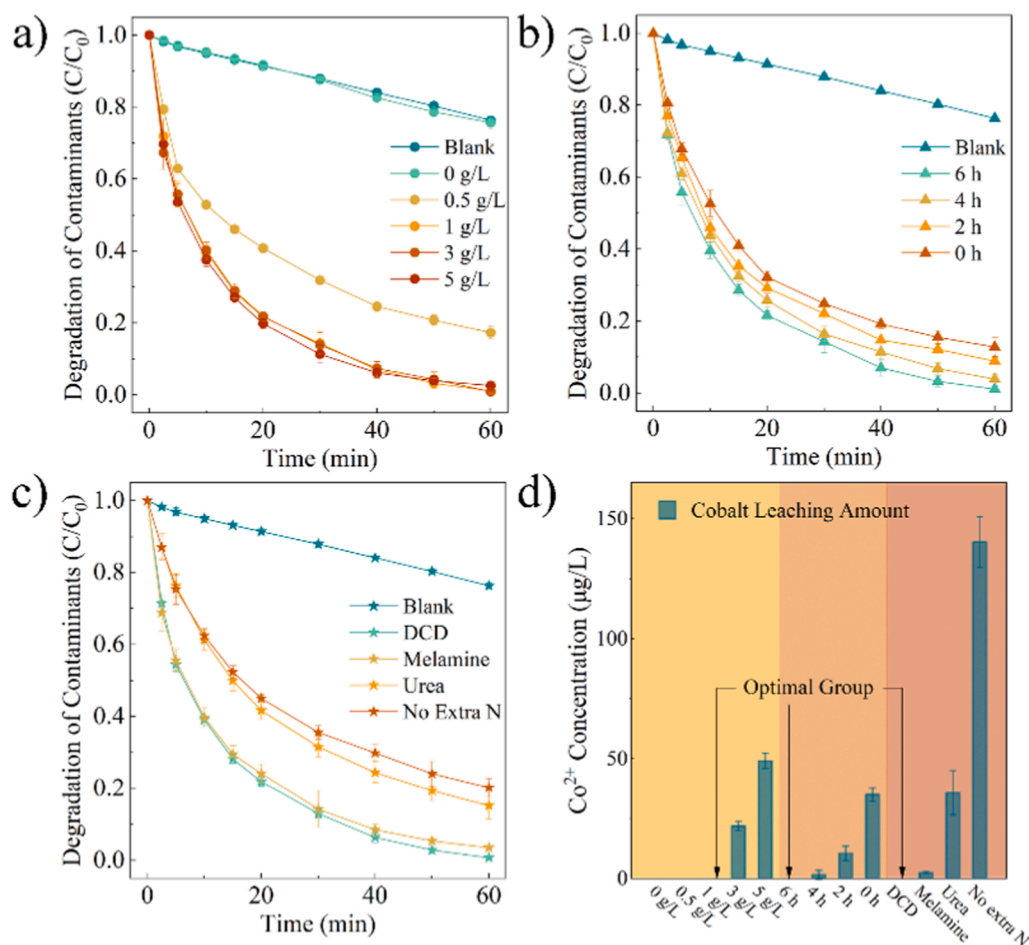


Fig. 3. Activation of peroxymonosulfate (PMS) to degrade sulfadoxin. Performance of Co-biochar catalysts synthesized under different conditions: (a) initial concentration for Co adsorption (0–5 g/L), (b) residence time of 550 °C heating (0–6 h), and (c) type of external N source (dicyandiamide (DCD), melamine, and urea). (d) Amounts of Co leached from the materials during the experiments. All of the preparation conditions deviated from the optimal conditions: 1 g/L initial Co concentration for adsorption, 0 h residence time of 550 °C heating, and DCD used as the external N source. Experimental conditions: [PMS] = 0.5 mM, [catalyst] = 100 mg/L, and [sulfadoxin] = 50 mM.

reached 5 g/L, the degradation performance was still no better than that for the optimal Co concentration of 1 g/L. For the residence time of 550 °C heating (0–6 h), the degradation performance gradually decreased with decreasing residence time. The degradation rate decreased from 100 % (6 h) to 80 % (0 h) in 60 min. When the residence time was over 4 h, the degradation performance was acceptable, indicating that only sufficient carbonization time can generate efficient Co-SA materials. Selection of the external N source is also important. Among the external N sources considered, melamine exhibited the same effect as DCD, while urea showed inferior performance. Melamine can also form C_3N_4 by carbonization at 550 °C, while urea is too volatile to be suitable [42]. Therefore, it can be inferred that C_3N_4 as the intermediate plays a critical role in construction of Co-SA sites. When no extra N was added for calcination, the degradation performance decreased, and it was concluded that the number of Co-SA sites determined the performance of the material. The amounts of Co leached from the materials are shown in Fig. 3d. Higher initial Co concentration caused more Co loss, indicating that 1 g/L reached the limit for SA-site generation. Shorter residence time, and especially the absence of the C_3N_4 intermediate, resulted in high Co leaching, suggesting that the reaction time of C_3N_4 played the role of stabilizing the Co sites during PMS activation.

Generation of Co SAs under the optimal preparation conditions was thus demonstrated, and changing the preparation conditions caused unsatisfactory performance, which was attributed to generation of NPs and the instability of the SA sites. However, the trends of SA and NP generation in regulation of the preparation conditions and the causes of the trends still require further investigation. To investigate the three influencing factors in Co-SA preparation, samples prepared under the

extreme conditions (5 g/L initial concentration for Co adsorption (Co-Ref1), 0 h residence time for 550 °C heating (Co-Ref2), and no extra N source addition (Co-NP) were chosen, with the other conditions chosen to be the optimal conditions) were used as control groups for comparison. The XRD patterns of Co-SA and the reference groups are shown in Fig. 4a. They showed a broad peak located at 25.2° , corresponding to the graphitic C (200) plane [43]. Peaks at $2\theta = 44.1^\circ$, 51.4° , and 75.8° were detected for Co-Ref1, Co-Ref2, and Co-NP, which are assigned to the (111), (200), and (220) planes of zero-valent cubic-phase cobalt (Co^0) (#JCPDS 15-0806) [44], where the material with no N addition showed the most intense Co^0 peaks. The magnetic properties of the materials, corresponding to Co^0 , were detected by VSM. The magnetic hysteresis loop from $-20,000$ to $20,000$ Oe are shown in Fig. 4b. Co-Ref1 and Co-Ref2 were magnetically positive, Co-NP had the strongest magnetism, and Co-SA showed no magnetic response, which was consistent with the XRD results [45]. Because 1 g/L initial Co concentration guaranteed well-dispersed SA sites, more Co for adsorption presumably did not lead to generation of more SA sites (comparing the XRD patterns of Co-SA with Co-Ref1 in Fig. 4a). According to previous SEM results (Fig. S1), generation of NPs showed no enhancement of the degradation performance, which can be attributed to the advantage of SAs in PMS catalysis competition [46]. XPS was performed to further understand the chemical composition. The elemental compositions of the materials synthesized under different preparation conditions were similar (Fig. S2). The deconvoluted Co 2p level XPS spectra of Co-SA and Co-NP are shown in Fig. 4c. Peaks at binding energies of 793.5 and 780.3 eV were observed for Co-SA, which are attributed to Co 2p_{1/2} and Co 2p_{3/2} [47], while the peak located at 781.2 eV for Co-NP can be attributed to Co^0 . Deconvolution of Co 2p (Fig. S3), N 1s (Fig. S4), and C 1s (Fig. S5)

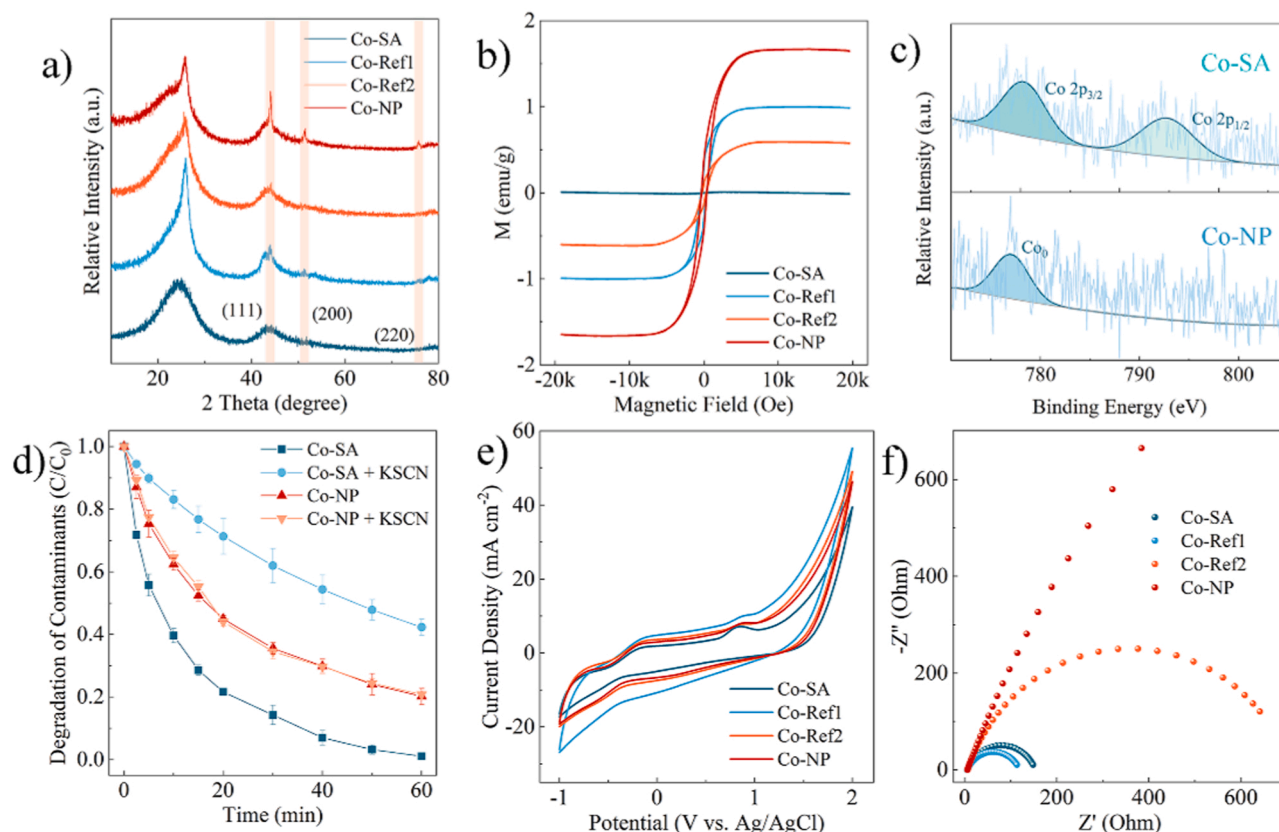


Fig. 4. a) X-ray diffraction patterns and b) vibrating sample magnetometry curves of the Co-biochar materials (Co-SA, Co-Ref1, Co-Ref2, and Co-NP). c) Comparison of the Co 2p X-ray photoelectron spectra of Co-SA and Co-NP. d) Poisoning effect of KSCN as the chelate agent on Co-SA sites (the catalysts were submerged in 0.5 M KSCN solution for 6 h). e) Cyclic voltammograms and f) electrochemical impedance spectra of the optimal and control group Co-biochar electrodes in 0.1 M Na₂SO₄ solution.

was performed for the optimal material and selected reference materials. The other two materials showed the same peaks as Co-SA in the Co 2p level spectra. For the C 1s level XPS spectra of all four materials, the peaks at 284.6, 258.7, and 287.9 eV are ascribed to C-C, C-N, and C-O bonds, respectively. The fitted peaks of the N 1s level were at 396.8, 398.1, 399.5, 400.7, 402.1, and 403.2 eV, corresponding to C-N, pyridinic N, Co-N, pyrrolic N, graphitic N, and oxidic N, respectively, where the material without N doping had no Co-N peak. Therefore, it was concluded that changing the preparation conditions led to Co⁰ NP (Co-NP) generation, especially when no external N was added, which resulted in a decrease of the degradation performance. According to the previous characterization results, Co-NP possibly only generated NPs and did not generate any SAs. This was verified using the ability of KSCN to poison Co SAs and negate their effect on catalyzing PMS [48]. The performance of Co-SA was almost eliminated, while KSCN did not affect the performance of the reference material (Co-NP) (Fig. 4d). The KSCN poisoning effect, and thus the SA distributions on Co-Ref1 and Co-Ref2, is shown in Fig. S6. Increasing the initial Co concentration for Co adsorption and decreasing the residence time for 550 °C heating decreased SA generation but enhanced NP generation, and only NPs and no SAs were generated when no extra N was added. Cyclic voltammetry and electrochemical impedance spectroscopy were performed to explain the change of electron transfer (Fig. 4e and f). Co-SA showed the lowest redox potential and the strongest redox peak, and Co-NP showed the highest redox potential and weakest redox peak, indicating that Co-SA had a lower energy input than Co-NP in PMS activation [49].

For Co-biochar materials, the preparation conditions not only influence generation of SAs and NPs, but they also determine the superficial properties. Raman spectroscopy was performed to investigate the number of defects in the biochar matrix of the materials prepared under

different preparation conditions (Fig. 5a). Two diagnostic peaks at 1350 cm⁻¹ (D band) and 1580 cm⁻¹ (G band) were identified, which are assigned to the vibrations of the sp³ hybridized orbit from defect and amorphous C atoms, and the sp² hybridized orbit from the ordered hexagonal lattice of graphite, respectively [50]. The ratio of the D band intensity to the G band intensity (I_D/I_G) is commonly used to analyze the defect and disorder degree of materials. The I_D/I_G values of the materials prepared under the optimal conditions, with an initial Co concentration of 5 g/L Co, with a residence time for 550 °C heating of 0 h, and with no extra N doping were 1.10, 1.08, 1.06, and 0.98, respectively. Therefore, generation of more Co SAs and fewer Co NPs was consistent with the defect number according to the previous characterization results. [14] The FTIR spectra of all of the materials showed peaks located at 3436, 1630, and 1420 cm⁻¹ (Fig. 5b), corresponding to stretching of the hydroxyl, carbonyl, and methyl groups, respectively [51]. The difference of the preparation conditions showed no obvious effect on the types of peaks, indicating that the surface and defects were stable through the whole as-configured calcination process. Furthermore, the nitrogen adsorption-desorption isotherms were determined by the BET method (Fig. 5c). All of the isotherms of the materials could be categorized as type IV with type-H3 hysteresis loops, indicating that they were mesoporous materials, and the selected changes of the preparation conditions did not necessarily affect the surface properties [52]. In addition, the pore-size distributions confirmed the mesoporous structures of the Co-biochar materials, with pore sizes ranging from 4.1 to 6.4 nm (Fig. 5d). The BET specific surface areas (S_{BET}), total pore volumes (V_t), and average pore diameters (D) of the optimal material and reference materials are given in Table S4. S_{BET} was greatly enhanced by external N addition, but Co-Ref2 surprisingly showed the highest S_{BET} value. The smaller surface area of the optimal material was presumably because of

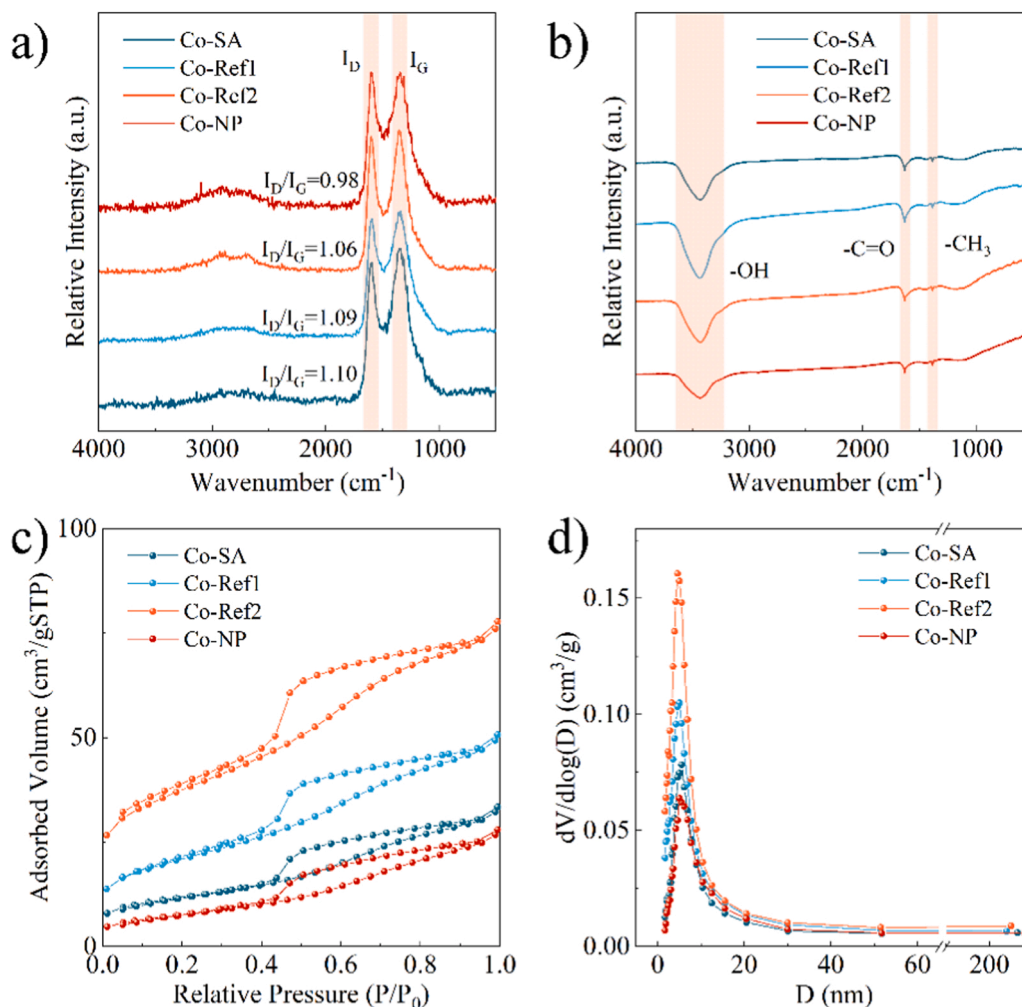


Fig. 5. a) Raman spectra, b) Fourier-transform infrared spectra, c) nitrogen adsorption-desorption isotherms, and d) pore-size distributions of the optimal and control group Co-biochar materials.

collapse of the biochar matrix during long-time melting and rearrangement. Combined with the previous characterization results, the surface properties did not match the catalytic performance, which was independent of material synthesis.

In summary, changing the selected preparation conditions regulated generation of SA and NP sites on the biochar. The optimal preparation conditions exclusively resulted in generation of SAs, while excessive adsorbed Co generated NPs despite the existence of SAs. Shorter residence time for 550 °C heating generated NPs with SAs, and the absence of external N resulted in generation of only NPs.

3.3. Different activation pathways of single atoms and nanoparticles

Deviation from the optimal preparation conditions caused a difference in the active sites and composition ratio of SAs and NPs on the material in PMS activation. Therefore, quenching experiments were carried out to identify the types and amounts of the radical and non-radical species, revealing how the change in the Co form changed the activation mechanism of the catalyst in the PMS system. Suitable quenching agents were used to investigate the activation mechanism. Methanol (MeOH) was used for quenching both $\cdot\text{OH}$ and $\text{SO}_4^{\cdot-}$, with rapid quenching rates of $1.9 \times 10^9 \text{ M}^{-1} \text{ s}^{-1}$ and $3.5 \times 10^7 \text{ M}^{-1} \text{ s}^{-1}$, respectively [53]. *Tert*-butyl alcohol (*t*-BA) can effectively scavenge $\cdot\text{OH}$ with a reaction rate constant of $3.8\text{--}7.6 \times 10^8 \text{ M}^{-1} \text{ s}^{-1}$, but it also moderately quenches $\text{SO}_4^{\cdot-}$ with a reaction rate constant of $4.0\text{--}9.1 \times 10^5 \text{ M}^{-1} \text{ s}^{-1}$ [54]. $^1\text{O}_2$ is the most common non-radical active species in PMS

treatment, triggering strong oxidation of organic contaminants as another mechanism, which can be quenched by a small amount of FFA [55]. Co=O is also a potential active species in PMS degradation, which can be scavenged by PMSO and generate the characteristic product PMSO_2 [56]. The optimal concentrations of the various scavengers were selected to investigate the effects of the reactive species. The detailed results are shown in Fig. S7, and the extracted pseudo-first-order kinetics reaction rates (k_{obs}) are summarized in Fig. 6a. MeOH, *t*-BA, and FFA showed little inhibition of degradation, while PMSO almost stopped the reaction of Co-SA, indicating that the oxidation pathway of Co-SA/PMS was dominated by Co=O . Co-NP showed a totally different mechanism, with PMSO unable to quench the reaction, but FFA effective terminating the reaction, suggesting that aqueous $^1\text{O}_2$ was the most effective active species in the Co-NP/PMS system accompanied by a much less intense radical pathway. For Co-Ref1/PMS and Co-Ref2/PMS, a mixed oxidation mechanism was shown, which can be explained by the fact that the NPs removed a portion of PMS that should have been utilized by SAs. Therefore, in Co/PMS heterogeneous activation, the SAs generated Co=O and the NPs mainly generated $^1\text{O}_2$ with a small amount of radicals for contaminant oxidation.

PMSO can also be used as the probe of the active species, and the Co=O species was verified by mass analysis of PMSO and its oxidation product PMSO_2 (Fig. 6e and f). Consumption of PMSO and generation of PMSO_2 were correlated with the PMSO quenching degree (Fig. 6d) [56]. The Co-NP/PMS system was limited in terms of PMSO conversion, while the optimal material and other two reference materials were able to

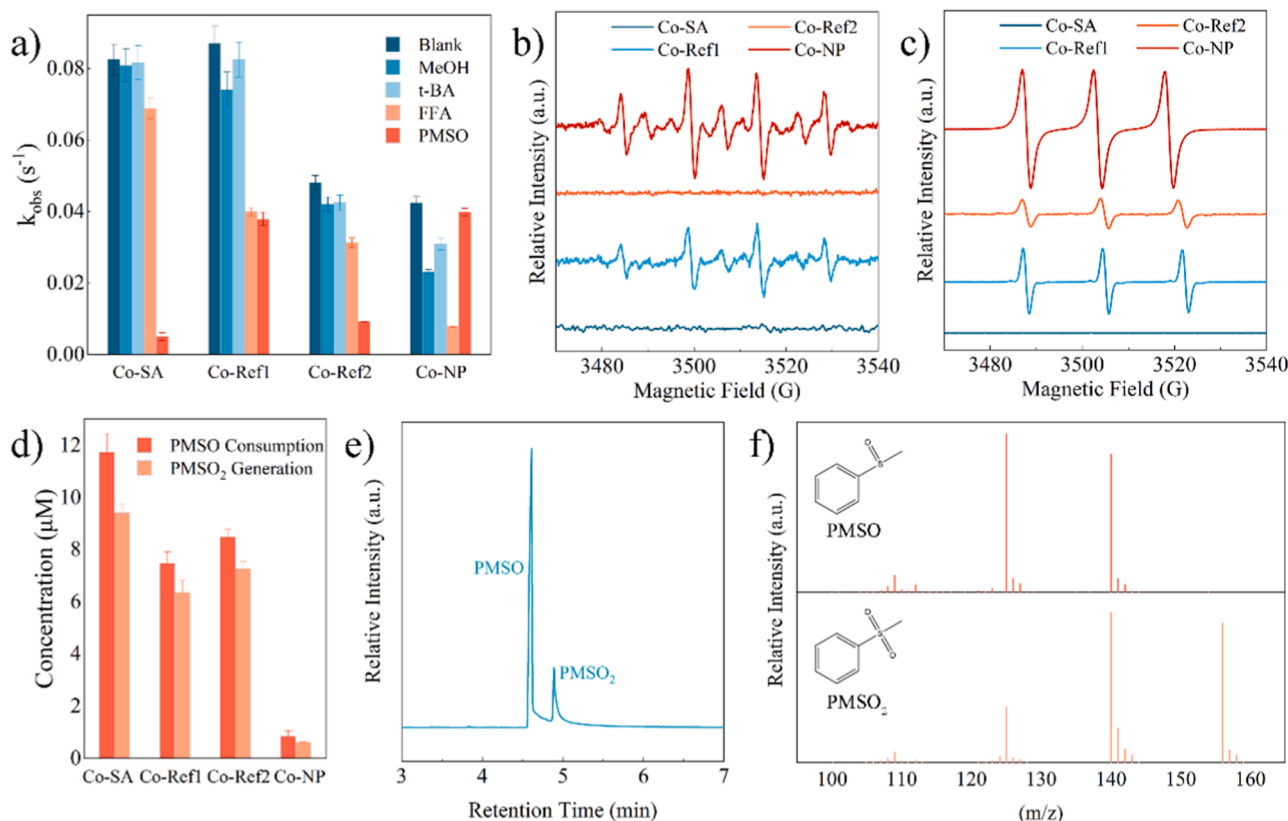


Fig. 6. a) Effects of different quenching agents on the Co-biochar materials (Co-SA, Co-Ref1, Co-Ref2, and Co-NP) (contaminant [sulfadoxin] = 50 mM, [MeOH] = 500 mM, [t-BA] = 500 mM, [FFA] = 5 mM, and [PMSO] = 5 mM). b) PMSO consumption and PMSO₂ generation in the different catalytic systems. Electron paramagnetic resonance spectra with trapping agents of c) DMPO and d) TEMP for the different catalytic systems. e) Total ion chromatograms and f) mass spectra of PMSO and its characteristic oxidation product PMSO₂ in the Co-SA/PMS system.

transform up to 11.8 μM of PMSO. In accordance with the quenching experiments, Co-SA generated no aqueous radical or non-radical species in PMS activation but anchored the Co=O species, while Co-NP mainly generated 1O_2 with small amounts of $\cdot OH$ and $SO_4^{\cdot -}$. To verify the previous results, electron paramagnetic resonance (EPR) was performed with the trapping agents DMPO and TEMP. The signals of DMPO as the trapping agent for $\cdot OH$ and $SO_4^{\cdot -}$ were detected in the EPR tests. Signals with an intensity ratio of 1:2:2:1 representing the DMPO- $\cdot OH$ and DMPO- $SO_4^{\cdot -}$ adducts were only detected for Co-NP and Co-Ref1 [57]. All of the materials except for Co-SA showed signals with an intensity ratio of 1:1:1, which are attributed to the existence of 1O_2 in PMS activation (Fig. 6c) [58].

To verify that the Co-SA/PMS system generated the anchored Co=O species for interface oxidation while Co-NP/PMS generated the aqueous oxygen species, PMS decomposition was investigated for the Co-SA/PMS, Co-Ref1/PMS, Co-Ref2/PMS, and Co-NP/PMS systems (Fig. S8). Addition of Co-NP greatly enhanced PMS consumption even without contaminants, while Co-SA alone could not enhance PMS decomposition without contaminants. The poisoning effect of KSCN was also considered. The results showed that KSCN poisoning affected SA catalysis but had no obvious effect on NP catalysis, and the tendency of KSCN reacting with the oxidizer PMS was not observed.

Because the adaptability in aqueous environmental interference and the stability reflect the quality of SA sites [59], the superior performance of Co-SA to Co-NP demonstrated its adaptability and recyclability in PMS activation. In PMS treatment, extreme acidity can suppress PMS activation, while extreme alkalinity can enhance the oxidation effect [60]. The performance of Co-NP/PMS showed higher inhibition than that of Co-SA/PMS when the solution was acidic, and it improved more in an alkaline aqueous environment, indicating the higher stability of

Co-SA than Co-NP (Fig. 7a). Carbonate and phosphate ions decreased the degradation efficiency of Co-SA/PMS, while all of the considered ions affected the degradation efficiency of Co-NP/PMS, including chloride and nitrate ions that can easily generate the corresponding active species (Fig. 7b) [61,62]. The experiments of extreme pH and anion interference showed that the aqueous-oxidation-dominant Co-NP/PMS system is more likely to be influenced by the pH and anions than the interface-reaction-dominant Co-SA/PMS system. Aqueous active species are greatly affected by the aqueous environment, which limits potential applications of Co-NP. The results of recyclability tests are shown in Fig. 7c. Both systems showed loss of performance after four cycles, but Co-SA showed less degeneration, presumably because of its powerful catalytic ability. The quantified catalysis attenuation is shown in Fig. S9. The PMS activation mechanisms on the SA and NP sites diverged into two completely different mechanisms, which shows that the SA-derived active species could have higher adaptability to aqueous interference.

3.4. Mechanisms and effectiveness of different activation pathways

To determine the reason why Co-SA/PMS generated anchored the Co=O species while Co-NP/PMS generated 1O_2 as the most effective oxidant, the processes of PMS adsorbing on the Co-SA and Co-NP surfaces and cleaving to generate Co=O species were simulated, and the free energies of each stage were calculated to investigate the feasibility of generating interface oxidation species on the material surfaces (Fig. 8a). According to the previous characterization results, Co-N₄ was chosen as the structure of Co-SA and Co (100) was chosen as the exposed plane of Co-NP. The whole process is described as PMS adsorption on the material, PMS cleavage to generate an adsorbed O atom and dissociated HSO₄ group, and desorption of the anchored O atom. Compared with Co-

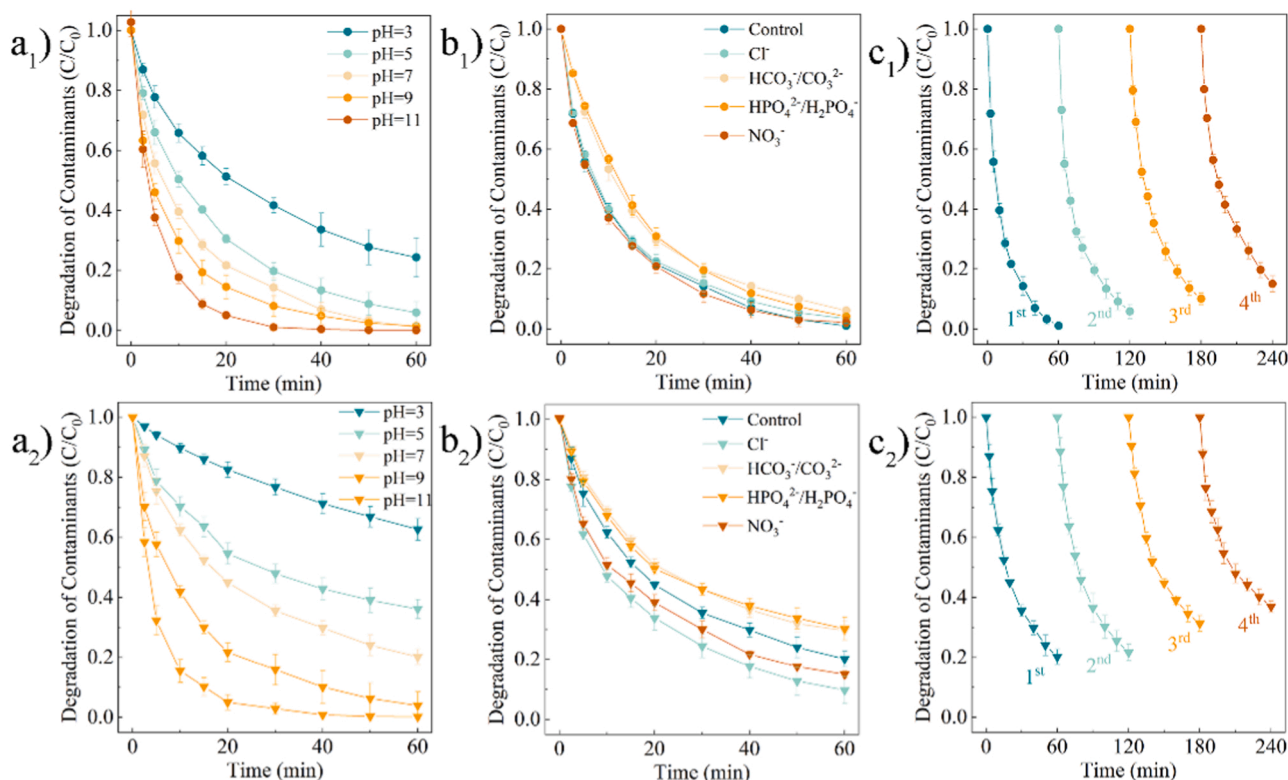


Fig. 7. Adaptability and stability of the a₁)–a₃) Co-SA and b₂)–b₃) Co-NP catalysts. a) Interference by the pH, b) interference by disturbing ions ($[\text{Cl}^-] = [\text{HCO}_3^-/\text{CO}_3^{2-}] = [\text{HPO}_4^{2-}/\text{H}_2\text{PO}_4^-] = [\text{NO}_3^-] = 5 \text{ mM}$, pH = 7), and c) cycling experiments. Experimental conditions: [PMS] = 0.5 mM, [catalyst] = 100 mg/L, and [sulfadoxin] = 50 mM.

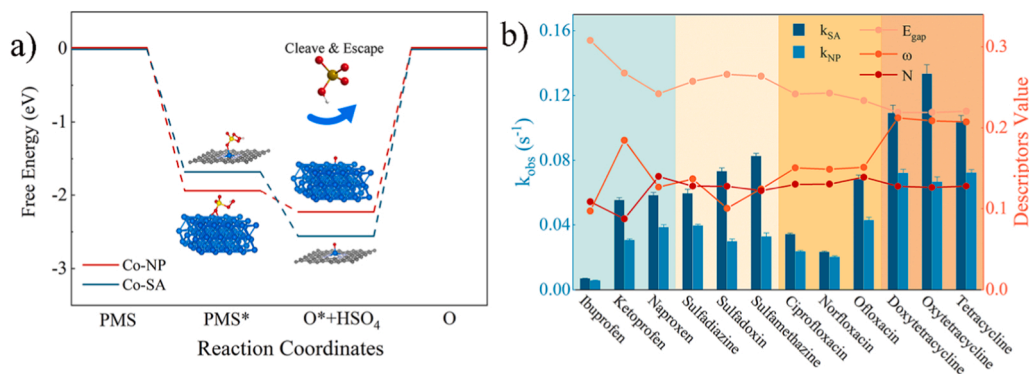


Fig. 8. a) Calculated free energy pathways of PMS adsorption and cleavage on the Co-NP and Co-SA surfaces. The inserts show the atomic structures of each stage of adsorption and cleavage of PMS on the different surfaces. b) Degradation rates (k_{obs}) of Co-SA/PMS and Co-NP/PMS, and the energy gap (E_{gap}), nucleophilic index (ω), and electrophilic index (N) values of different contaminants.

SA, PMS more easily adsorbed on Co-NP (−1.68 eV vs. −1.94 eV), but it was more difficult to cleave PMS to generate an anchored O atom and dissociated HSO₄ group (−0.29 eV vs. −0.88 eV). The as-formed anchored O atom existed more stably on Co-SA than on Co-NP (2.23 eV vs. 2.56 eV), demonstrating its higher accessibility for generating Co=O. Therefore, the results of the theoretical calculations directly showed that Co-SA more easily activates adsorbed PMS to generate an anchored O atom on the material surface. According to detection of the active species, the higher tendency for O atom desorption presumably results in formation of aqueous ¹O₂.

To further investigate the oxidation effects of Co=O and ¹O₂, 12 different contaminants were selected (three from each of the profen, sulfanilamide, quinolone, and tetracycline groups, Table S1) for degradation by the Co-SA/PMS and Co-NP/PMS systems. The degradation

performance is shown in Fig. S10, and the derived pseudo-first-order kinetics parameters are shown in Fig. 8b. To understand the difference of the degradation performance, the geometrical structures of the contaminants were optimized and the molecular descriptors (energy gap E_{gap} , nucleophilic index ω , and electrophilic index N) were calculated (Fig. S11). Generally, Co-SA/PMS showed superior performance to Co-NP/PMS. The tetracyclines showed the highest degradation, while the profens and quinolones showed relatively low degradation. An increase of E_{gap} and a decrease of ω corresponded to a decrease of k_{obs} , indicating that the degradation reactions triggered by ¹O₂ and Co=O could be electrophilic, and E_{gap} reflected the vulnerability of the contaminants to degradation. The differences between the k_{obs} values of the Co-SA/PMS and Co-NP/PMS systems were relatively large for the profens and quinolones, which was consistent with the differences between the ω

and N values. This is presumably because $\text{Co}=\text{O}$ is more likely to trigger electrophilic reactions than $^1\text{O}_2$.

The degradation pathways of sulfadoxin are proposed, and the main intermediate oxidation products were compared to further understand the difference in the oxidation effects of the Co-SA/PMS and Co-NP/PMS systems. The proposed pathways are shown in Fig. 9a, and the gas chromatography results and mass spectra are shown in Figs. S12–S17. Six intermediate products, namely, P155, P246, P276, P310, P326, and P340 (including residual sulfadoxin), were considered for identification and quantification (the detailed information is given in Table S5). Generation of P340 is correlated with the amino oxidation reaction [63]. In Co-SA/PMS degradation, the P340 intermediate outweighed that in Co-NP/PMS degradation, indicating that the amino oxidation reaction is more likely to occur with $\text{Co}=\text{O}$. In Co-NP/PMS degradation, more P155 and P246 were generated than in Co-SA/PMS degradation, indicating that $^1\text{O}_2$ better induces S–N bond cleavage and SO_2 extrusion than $\text{Co}=\text{O}$ [64]. Generation of more P246 in the $^1\text{O}_2$ -dominated Co-NP/PMS system can be explained by $^1\text{O}_2$ acting as an electron donor and triggering “smiles” rearrangement of sulfa drugs [65]. Generation of P276 was approximately the same in the Co-SA/PMS and Co-NP/PMS systems. According to the proposed pathways, P276 can be generated in two different ways, but both require amino oxidation and SO_2 extrusion. These symmetrical pathways composed of the same reactions presumably resulted in equivalent generation of the intermediate product. For P326 generation by hydroxyl substitution, the Co-SA/PMS and Co-NP/PMS systems showed a similar effect, probably because all O-containing active species ($\cdot\text{OH}$, $\text{SO}_4^{\cdot-}$, $^1\text{O}_2$, and $\text{Co}=\text{O}$ in this study) can trigger hydroxyl substitution on the benzene ring [61]. Additionally, the environmental risks of the six intermediate products were clarified by the ECOSAR software package, and the results are shown in Fig. 9b. P155, P246, and P326, the intermediates more easily generated by Co-NP/PMS than by Co-SA/PMS, showed similar ecotoxicity to the original contaminant (P310), while P276 and P340, which are generated by amino oxidation from P246 and P340, respectively, showed lower ecotoxicity than the other intermediate products. The results indicated that in sulfadoxin oxidation, Co-SA/PMS is more likely to generate intermediate products with less environmental risk, while Co-NP/PMS generates intermediates with equivalent ecotoxicity to sulfadoxin itself, which shows that the oxidation process of the Co-SA/PMS system is safer than that of the Co-NP/PMS system. Consequently, Co-SA/PMS showed better performance in terms of both the degradation efficiency and environmental safety for antibiotic removal, demonstrating the advantages of the oxidation pathway induced by anchored $\text{Co}=\text{O}$

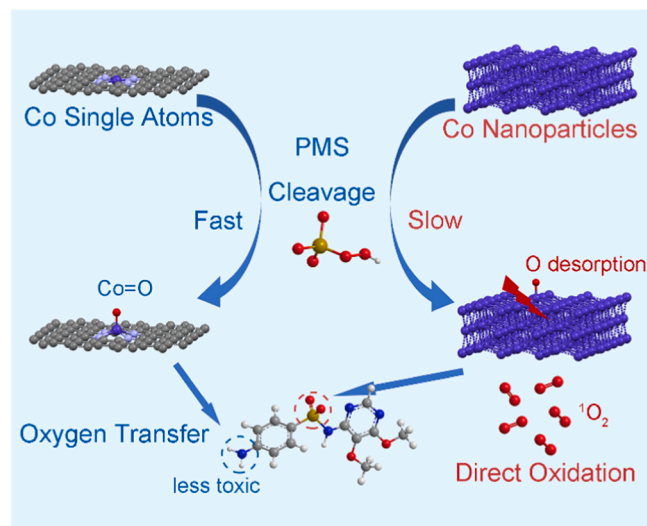


Fig. 10. Schematic illustration of this work.

compared with the oxidation pathway induced by aqueous oxygen species.

4. Conclusion

In this study, Co-SA sites were successfully created on a biochar matrix through two-step calcination, providing an effective PMS activator for antibiotic degradation. Synthesis of Co SAs and NPs was performed on the matrix by changing the preparation conditions of cobalt adsorption, the heating time, and the external nitrogen source. Optimal Co-SA and pure Co-NP materials were successfully fabricated for comprehensive comparison. In PMS activation for contaminant degradation, Co-SA showed superior degradation efficiency, adaptability, and stability to Co-NP. The performance differences between the Co-SA/PMS and Co-NP/PMS systems were explained. Anchored $\text{Co}=\text{O}$ was the reactive species in the Co-SA/PMS system, while aqueous radicals and non-radicals played dominant roles in the Co-NP/PMS system. Theoretical calculations showed that it was more difficult for Co NPs to retain anchored $\text{Co}=\text{O}$ species than Co SAs, and thus they could not trigger interface oxidation, which explained the change in the activation mechanism. Furthermore, degradation of various contaminants and

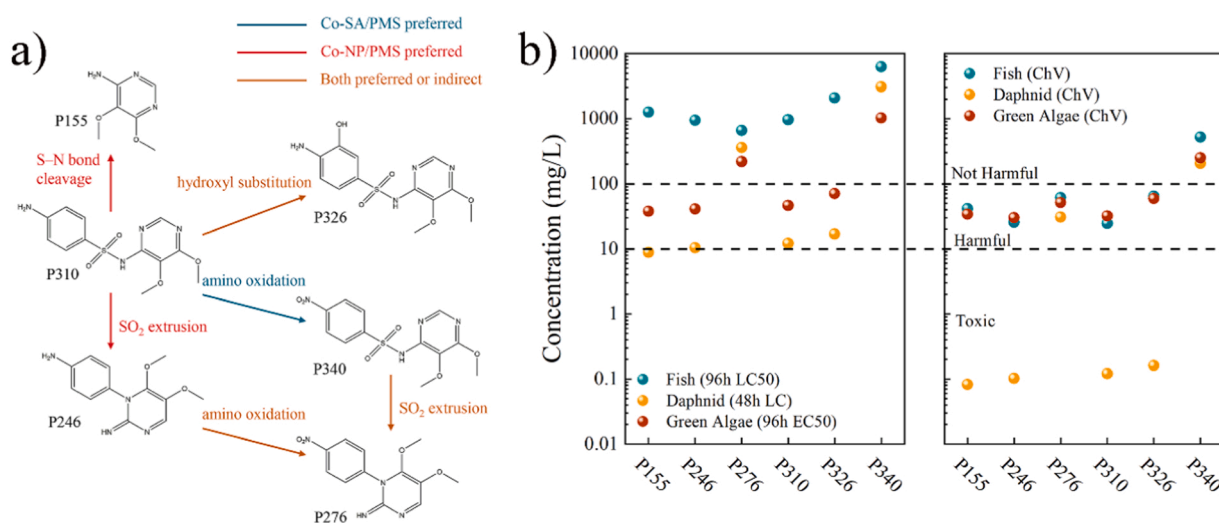


Fig. 9. a) Proposed degradation pathways of sulfadoxin and the corresponding preferred degradation systems for generation. b) Acute or chronic environmental risks of selected byproducts.

various sulfadoxin degradation pathways were investigated to analyze the different degradation effects and environmental safety of the Co-SA/PMS and Co-NP/PMS systems. Overall, by fabricating the Co-SA material as a PMS activator, the anchored Co=O species was generated for antibiotic degradation, and it showed superior performance to the aqueous oxygen species in the Co-NP/PMS system. The activation mechanisms and degradation effects of different oxidation pathways were accordingly elucidated, providing new insights into PMS-based catalytic systems for antibiotic treatment.

CCRediT authorship contribution statement

Zi-Jie Xiao: Investigation, Methodology, Validation, Formal analysis, Writing – original draft. **Bai-Qin Zhou:** Methodology, Formal analysis. **Xiao-Chi Feng:** Conceptualization, Resources, Writing – review & editing, Supervision, Project administration, Funding acquisition. **Hong-Tao Shi:** Data curation, Formal analysis. **Yi-Ning Zhu:** Methodology, Formal analysis. **Cai-Peng Wang:** Data curation. **Bart Van der Bruggen:** Writing – review & editing. **Nan-Qi Ren:** Writing – review & editing, Supervision, Funding acquisition.

Declaration of Competing Interest

The authors declare that they have no known competing financial interests or personal relationships that could have appeared to influence the work reported in this paper.

Data Availability

Data will be made available on request.

Acknowledgement

This investigation was funded by Guangdong Basic and Applied Basic Research Foundation (No. 2023A1515012383), State Key Laboratory of Urban Water Resource and Environment (Harbin Institute of Technology) (No. 2021TS30) and Shenzhen Science and Technology Program (KQTD20190929172630447, and KCXFZ20211020163404007).

Appendix A. Supporting information

Supplementary data associated with this article can be found in the online version at [doi:10.1016/j.apcatb.2023.122483](https://doi.org/10.1016/j.apcatb.2023.122483).

References

- [1] J. Lee, U. von Gunten, J.-H. Kim, Persulfate-based advanced oxidation: critical assessment of opportunities and roadblocks, *Environ. Sci. Technol.* 54 (2020) 3064–3081.
- [2] U. von Gunten, Oxidation processes in water treatment: are we on track? *Environ. Sci. Technol.* 52 (2018) 5062–5075.
- [3] J.L. Wang, S.Z. Wang, Activation of persulfate (PS) and peroxymonosulfate (PMS) and application for the degradation of emerging contaminants, *Chem. Eng. J.* 334 (2018) 1502–1517.
- [4] H. Wang, H. Xi, L.L. Xu, M.K. Jin, W.L. Zhao, H.J. Liu, Ecotoxicological effects, environmental fate and risks of pharmaceutical and personal care products in the water environment: a review, *Sci. Total Environ.* 788 (2021), 147819.
- [5] F. Ghanbari, M. Moradi, Application of peroxymonosulfate and its activation methods for degradation of environmental organic pollutants: review, *Chem. Eng. J.* 310 (2017) 41–62.
- [6] P.D. Hu, M.C. Long, Cobalt-catalyzed sulfate radical-based advanced oxidation: a review on heterogeneous catalysts and applications, *Appl. Catal. B-Environ.* 181 (2016) 103–117.
- [7] B.C. Hodges, E.L. Cates, J.-H. Kim, Challenges and prospects of advanced oxidation water treatment processes using catalytic nanomaterials, *Nat. Nanotechnol.* 13 (2018) 642–650.
- [8] Y. Liu, L. Liu, Y. Wang, A critical review on removal of gaseous pollutants using sulfate radical-based advanced oxidation technologies, *Environ. Sci. Technol.* 55 (2021) 9691–9710.
- [9] G.P. Anipsitakis, D.D. Dionysiou, Radical generation by the interaction of transition metals with common oxidants, *Environ. Sci. Technol.* 38 (2004) 3705–3712.
- [10] Y.B. Ding, X.R. Wang, L.B. Fu, X.Q. Peng, C. Pan, Q.H. Mao, C.J. Wang, J.C. Yan, Nonradicals induced degradation of organic pollutants by peroxydisulfate (PDS) and peroxymonosulfate (PMS): recent advances and perspective, *Sci. Total Environ.* 765 (2021), 142794.
- [11] Y. Zong, H. Zhang, X.M. Zhang, W. Liu, L.Q. Xu, D.L. Wu, High-valent cobalt-oxo species triggers hydroxyl radical for collaborative environmental decontamination, *Appl. Catal. B-Environ.* 300 (2022), 120722.
- [12] E.T. Yun, J.H. Lee, J. Kim, H.D. Park, J. Lee, Identifying the nonradical mechanism in the peroxymonosulfate activation process: singlet oxygenation versus mediated electron transfer, *Environ. Sci. Technol.* 52 (2018) 7032–7042.
- [13] X.-C. Feng, Z.-J. Xiao, H.-T. Shi, B.-Q. Zhou, Y.-M. Wang, H.-Z. Chi, X.-H. Kou, N.-Q. Ren, How nitrogen and sulfur doping modified material structure, transformed oxidation pathways, and improved degradation performance in peroxymonosulfate activation, *Environ. Sci. Technol.* 56 (2022) 14048.
- [14] Z.-J. Xiao, X.-C. Feng, H.-T. Shi, B.-Q. Zhou, W.-Q. Wang, N.-Q. Ren, Why the cooperation of radical and non-radical pathways in PMS system leads to a higher efficiency than a single pathway in tetracycline degradation, *J. Hazard. Mater.* 424 (2022), 127247.
- [15] J.B. Xi, H.S. Jung, Y. Xu, F. Xiao, J.W. Bae, S. Wang, Synthesis strategies, catalytic applications, and performance regulation of single-atom catalysts, *Adv. Funct. Mater.* 31 (2021) 2008318.
- [16] X. Li, X. Huang, S. Xi, S. Miao, J. Ding, W. Cai, S. Liu, X. Yang, H. Yang, J. Gao, J. Wang, Y. Huang, T. Zhang, B. Liu, Single cobalt atoms anchored on porous N-doped graphene with dual reaction sites for efficient fenton-like catalysis, *J. Am. Chem. Soc.* 140 (2018) 12469–12475.
- [17] H. Xu, N. Jiang, D. Wang, L. Wang, Y. Song, Z. Chen, J. Ma, T. Zhang, Improving PMS oxidation of organic pollutants by single cobalt atom catalyst through hybrid radical and non-radical pathways, *Appl. Catal. B: Environ.* 263 (2020), 118350.
- [18] X.M. Peng, J.Q. Wu, Z.L. Zhao, X. Wang, H.L. Dai, L. Xu, G.P. Xu, Y. Jian, F.P. Hu, Activation of peroxymonosulfate by single-atom Fe-g-C₃N₄ catalysts for high efficiency degradation of tetracycline via nonradical pathways: role of high-valent iron-oxo species and Fe-Nx sites, *Chem. Eng. J.* 427 (2022), 130803.
- [19] K. Qian, H. Chen, W.L. Li, Z.M. Ao, Y.N. Wu, X.H. Guan, Single-atom Fe catalyst outperforms its homogeneous counterpart for activating peroxymonosulfate to achieve effective degradation of organic contaminants, *Environ. Sci. Technol.* 55 (2021) 7034–7043.
- [20] Y. Li, T. Yang, S.H. Qiu, W.Q. Lin, J.T. Yan, S.S. Fan, Q. Zhou, Uniform N-coordinated single-atomic iron sites dispersed in porous carbon framework to activate PMS for efficient BPA degradation via high-valent iron-oxo species, *Chem. Eng. J.* 389 (2020), 124382.
- [21] Z.C. Wu, C.L. Wang, Z. Luo, Y. Qin, X.S. Wang, J. Wen, L.Y. Hu, W.L. Gu, C.Z. Zhu, Peroxymonosulfate activation on synergistically enhanced single-atom Co/Co@C for boosted chemiluminescence of tris(bipyridine) ruthenium(II) derivative, *Anal. Chem.* 94 (2022) 6866–6873.
- [22] W.H. Ren, X. Tan, C. Jia, A. Krammer, Q. Sun, J.T. Qu, S.C. Smith, A. Schueler, X. L. Hu, C. Zhao, Electronic regulation of nickel single atoms by confined nickel nanoparticles for energy-efficient CO₂ electroreduction, *Angew. Chem. Int. Ed.* 61 (2022), e202203335.
- [23] L.M. Jin, S.J. You, Y. Yao, H. Chen, Y. Wang, Y.B.A. Liu, An electroactive single-atom copper anchored MXene nanohybrid filter for ultrafast water decontamination, *J. Mater. Chem. A* 9 (2021) 25964–25973.
- [24] X.Y. Mi, P.F. Wang, S.Z. Xu, L.N. Su, H. Zhong, H.T. Wang, Y. Li, S.H. Zhan, Almost 100 % peroxymonosulfate conversion to singlet oxygen on single-atom CoN₂+2 sites, *Angew. Chem. Int. Ed.* 60 (2021) 4588–4593.
- [25] Y. Zhao, D.G. Truhlar, The M06 suite of density functionals for main group thermochemistry, thermochemical kinetics, noncovalent interactions, excited states, and transition elements: two new functionals and systematic testing of four M06-class functionals and 12 other functionals, *Theor. Chem. Acc.* 120 (2008) 215–241.
- [26] F. Weigend, R. Ahlrichs, Balanced basis sets of split valence, triple zeta valence and quadruple zeta valence quality for H to Rn: design and assessment of accuracy, *Phys. Chem. Chem. Phys.* 7 (2005) 3297–3305.
- [27] A.V. Marenich, C.J. Cramer, D.G. Truhlar, Universal solvation model based on solute electron density and on a continuum model of the solvent defined by the bulk dielectric constant and atomic surface tensions, *J. Phys. Chem. B* 113 (2009) 6378–6396.
- [28] G. Kresse, J. Furthmüller, Efficient iterative schemes for ab initio total-energy calculations using a plane-wave basis set, *Phys. Rev. B* 54 (1996) 11169–11186.
- [29] G. Kresse, J. Furthmüller, Efficiency of ab-initio total energy calculations for metals and semiconductors using a plane-wave basis set, *Comput. Mater. Sci.* 6 (1996) 15–50.
- [30] J.P. Perdew, K. Burke, Y. Wang, Generalized gradient approximation for the exchange-correlation hole of a many-electron system, *Phys. Rev. B* 54 (1996) 16533–16539.
- [31] H.J. Monkhorst, J.D. Pack, Special points for Brillouin-zone integrations, *Phys. Rev. B* 13 (1976) 5188–5192.
- [32] P.E. Blöchl, Projector augmented-wave method, *Phys. Rev. B* 50 (1994) 17953–17979.
- [33] S. Grimme, J. Antony, S. Ehrlich, H. Krieg, A consistent and accurate ab initio parametrization of density functional dispersion correction (DFT-D) for the 94 elements H-Pu, *J. Chem. Phys.* 132 (2010), 154104.
- [34] X. Liu, Y. Deng, L. Zheng, M.R. Kesama, C. Tang, Y. Zhu, Engineering low-coordination single-atom cobalt on graphitic carbon nitride catalyst for hydrogen evolution, *ACS Catalysis* 12 (2022) 5517–5526.
- [35] E. Zhang, T. Wang, K. Yu, J. Liu, W. Chen, A. Li, H. Rong, R. Lin, S. Ji, X. Zheng, Y. Wang, L. Zheng, C. Chen, D. Wang, J. Zhang, Y. Li, Bismuth single atoms

- resulting from transformation of metal–organic frameworks and their use as electrocatalysts for CO₂ reduction, *J. Am. Chem. Soc.* 141 (2019) 16569–16573.
- [36] D. Zheng, C. Huang, X. Wang, Post-annealing reinforced hollow carbon nitride nanospheres for hydrogen photosynthesis, *Nanoscale* 7 (2015) 465–470.
- [37] F. Chen, X.L. Wu, C.Y. Shi, H.J. Lin, J.R. Chen, Y.P. Shi, S.B. Wang, X.G. Duan, Molecular engineering toward pyrrolic N-rich M–N–4 (M = Cr, Mn, Fe, Co, Cu) single-atom sites for enhanced heterogeneous fenton-like reaction, *Adv. Funct. Mater.* 31 (2021) 2007877.
- [38] D.X. Ji, L. Fan, L.L. Li, S.J. Peng, D.S. Yu, J.N. Song, S. Ramakrishna, S.J. Guo, Atomically transition metals on self-supported porous carbon flake arrays as binder-free air cathode for wearable zinc-air batteries, *Adv. Mater.* 31 (2019) 1808267.
- [39] W. Liu, L. Zhang, W. Yan, X. Liu, X. Yang, S. Miao, W. Wang, A. Wang, T. Zhang, Single-atom dispersed Co–N–C catalyst: structure identification and performance for hydrogenative coupling of nitroarenes, *Chem. Sci.* 7 (2016) 5758–5764.
- [40] P. Wang, Y. Ren, R. Wang, P. Zhang, M. Ding, C. Li, D. Zhao, Z. Qian, Z. Zhang, L. Zhang, L. Yin, Atomically dispersed cobalt catalyst anchored on nitrogen-doped carbon nanosheets for lithium-oxygen batteries, *Nat. Commun.* 11 (2020) 1576.
- [41] H. Tian, H. Tian, S. Wang, S. Chen, F. Zhang, L. Song, H. Liu, J. Liu, G. Wang, High-power lithium–selenium batteries enabled by atomic cobalt electrocatalyst in hollow carbon cathode, *Nat. Commun.* 11 (2020) 5025.
- [42] X. Wu, D. Gao, H. Yu, J. Yu, High-yield lactic acid-mediated route for a g-C₃N₄ nanosheet photocatalyst with enhanced H₂-evolution performance, *Nanoscale* 11 (2019) 9608–9616.
- [43] Y. Chen, J. Liu, Q. Zeng, Z. Liang, X. Ye, Y. Lv, M. Liu, Preparation of Eucommia ulmoides lignin-based high-performance biochar containing sulfonic group: synergistic pyrolysis mechanism and tetracycline hydrochloride adsorption, *Bioresour. Technol.* 329 (2021), 124856.
- [44] B.-T. Zhang, Y. Zhang, Y. Teng, Electrospun magnetic cobalt–carbon nanofiber composites with axis-sheath structure for efficient peroxymonosulfate activation, *Appl. Surf. Sci.* 452 (2018) 443–450.
- [45] S.R. Yousefi, H.A. Alshamsi, O. Amiri, M. Salavati-Niasari, Synthesis, characterization and application of Co/Co₃O₄ nanocomposites as an effective photocatalyst for discoloration of organic dye contaminants in wastewater and antibacterial properties, *J. Mol. Liq.* 337 (2021), 116405.
- [46] M. Farnesi Camellone, F. Dvořák, M. Vorokhta, A. Tovt, I. Khalakhan, V. Johánek, T. Skála, I. Matolínová, S. Fabris, J. Mysliveček, Atom and nanoparticle dynamics on single-atom catalyst substrates, *ACS Catal.* 12 (2022) 4859–4871.
- [47] T. Palaniselvam, V. Kashyap, S.N. Bhange, J.B. Baek, S. Kurungot, Nanoporous graphene enriched with Fe/Co–N active sites as a promising oxygen reduction electrocatalyst for anion exchange membrane fuel cells, *Adv. Funct. Mater.* 26 (2016) 2150–2162.
- [48] Q. Lu, C. Chen, Q. Di, W.L. Liu, X.H. Sun, Y.X. Tuo, Y. Zhou, Y. Pan, X. Feng, L. N. Li, D. Chen, J. Zhang, Dual role of pyridinic-N doping in carbon-coated Ni nanoparticles for highly efficient electrochemical CO₂ reduction to CO over a wide potential range, *Acs Catal.* 12 (2022) 1364–1374.
- [49] X.G. Duan, C. Su, J. Miao, Y.J. Zhong, Z.P. Shao, S.B. Wang, H.Q. Sun, Insights into perovskite-catalyzed peroxymonosulfate activation: maneuverable cobalt sites for promoted evolution of sulfate radicals, *Appl. Catal. B-Environ.* 220 (2018) 626–634.
- [50] S.J. Yu, X.X. Wang, W. Yao, J. Wang, Y.F. Ji, Y.J. Ai, A. Alsaedi, T. Hayat, X. K. Wang, Macroscopic, spectroscopic, and theoretical investigation for the interaction of phenol and naphthol on reduced graphene oxide, *Environ. Sci. Technol.* 51 (2017) 3278–3286.
- [51] K.B. Cantrell, P.G. Hunt, M. Uchimiya, J.M. Novak, K.S. Ro, Impact of pyrolysis temperature and manure source on physicochemical characteristics of biochar, *Bioresour. Technol.* 107 (2012) 419–428.
- [52] L. Ge, M. Zhang, R. Wang, N. Li, L.X. Zhang, S.F. Liu, T.F. Jiao, Fabrication of CS/GA/RGO/Pd composite hydrogels for highly efficient catalytic reduction of organic pollutants, *Rsc Adv.* 10 (2020) 15091–15097.
- [53] T. Zeng, X.L. Zhang, S.H. Wang, H.Y. Niu, Y.Q. Cai, Spatial confinement of a Co₃O₄ catalyst in hollow metal-organic frameworks as a nanoreactor for improved degradation of organic pollutants, *Environ. Sci. Technol.* 49 (2015) 2350–2357.
- [54] B.T. Zhang, Y. Zhang, Y.H. Teng, M.H. Fan, Sulfate radical and its application in decontamination technologies, *Crit. Rev. Environ. Sci. Technol.* 45 (2015) 1756–1800.
- [55] Y. Yang, G. Banerjee, G.W. Brudvig, J.H. Kim, J.J. Pignatello, Oxidation of organic compounds in water by unactivated peroxymonosulfate, *Environ. Sci. Technol.* 52 (2018) 5911–5919.
- [56] Y. Zong, X.H. Guan, J. Xu, Y. Feng, Y.F. Mao, L.Q. Xu, H.Q. Chu, D.L. Wu, Unraveling the overlooked involvement of high-valent cobalt-oxo species generated from the cobalt(II)-activated peroxymonosulfate process, *Environ. Sci. Technol.* 54 (2020) 16231–16239.
- [57] M. Ding, W. Chen, H. Xu, Z. Shen, T. Lin, K. Hu, C.H. Lu, Z. Xie, Novel alpha-Fe₂O₃/MXene nanocomposite as heterogeneous activator of peroxymonosulfate for the degradation of salicylic acid, *J. Hazard. Mater.* 382 (2020), 121064.
- [58] H.-B. Qiu, P.-C. Guo, L. Yuan, G.-P. Sheng, Different non-radical oxidation processes of persulfate and peroxymonosulfate activation by nitrogen-doped mesoporous carbon, *Chin. Chem. Lett.* 31 (2020) 2614–2618.
- [59] G.B. Chen, P. Liu, Z.Q. Liao, F.F. Sun, Y.H. He, H.X. Zhong, T. Zhang, E. Zschech, M.W. Chen, G. Wu, J. Zhang, X.L. Feng, Zinc-mediated template synthesis of Fe–N–C electrocatalysts with densely accessible Fe–N–x active sites for efficient oxygen reduction, *Adv. Mater.* 32 (2020) 1907399.
- [60] Y.-H. Guan, J. Ma, X.-C. Li, J.-Y. Fang, L.-W. Chen, Influence of pH on the formation of sulfate and hydroxyl radicals in the UV/peroxymonosulfate system, *Environ. Sci. Technol.* 45 (2011) 9308–9314.
- [61] W. Wang, Z. Chen, P. Yan, B. Wang, Y. Li, J. Kang, J. Shen, Y. Cheng, S. Wang, Y. Liu, Z. Wang, X. Li, Degradation of iopamidol by silicate-based microfiltration membrane activated peroxymonosulfate in aqueous solution: efficiency, mechanism and degradation pathway, *J. Clean. Prod.* 338 (2022), 130562.
- [62] K. Zhu, H. Jia, W. Jiang, Y. Sun, C. Zhang, Z. Liu, T. Wang, X. Guo, L. Zhu, The first observation of the formation of persistent aminoxyl radicals and reactive nitrogen species on photoirradiated nitrogen-containing microplastics, *Environ. Sci. Technol.* 56 (2022) 779–789.
- [63] X.L. Zou, T. Zhou, J. Mao, X.H. Wu, Synergistic degradation of antibiotic sulfadiazine in a heterogeneous ultrasound-enhanced Fe–O/persulfate Fenton-like system, *Chem. Eng. J.* 257 (2014) 36–44.
- [64] Y. Feng, D.L. Wu, Y. Deng, T. Zhang, K.M. Shih, Sulfate radical-mediated degradation of sulfadiazine by CuFeO₂ rhombohedral crystal-catalyzed peroxymonosulfate: synergistic effects and mechanisms, *Environ. Sci. Technol.* 50 (2016) 3119–3127.
- [65] A.L. Boreen, W.A. Arnold, K. McNeill, Triplet-sensitized photodegradation of sulfa drugs containing six-membered heterocyclic groups: identification of an SO₂ extrusion photoproduct, *Environ. Sci. Technol.* 39 (2005) 3630–3638.